
A Search for New Exotic Particles with Jets in Proton-Proton Collisions at the CMS Experiment

Dissertation

zur

**Erlangung der naturwissenschaftlichen Doktorwürde
(Dr. sc. nat.)**

vorgelegt der

Mathematisch-naturwissenschaftlichen Fakultät

der

Universität Zürich

von

Johnny B. Goode

aus

Deutschland

Promotionskommission

Prof. Dr. Ben Kilminster (Vorsitz)

Prof. Dr. Florencia Canelli

Prof. Dr. Nicola Serra

Prof. Dr. Gino Isidori

Zürich, 20...

Contents

Abstract	iii
Acknowledgements	iv
1 Introduction	1
2 The Standard Model	2
2.1 The Standard Model	2
2.1.1 The Standard Model Lagrangian	2
2.1.2 The gauge sector	2
2.1.3 The Yukawa sector	5
2.1.4 CKM matrix	5
2.2 Higgs	6
2.3 The physics of proton-proton collisions	6
3 Beyond the Standard Model	8
4 The CMS Experiment	10
4.1 The Large Hadron Collider	10
4.1.1 Luminosity	10
4.2 The CMS detector	12
4.2.1 Coordinate system	13
4.2.2 The solenoid magnet & flux-return yoke	13
4.2.3 The pixel tracker	13
4.2.4 The silicon strip tracker	13
4.2.5 The electromagnetic calorimeter	13
4.2.6 The hadronic calorimeter	13
4.2.7 The muon system	13
4.2.8 The trigger system	15
5 Object & Event Reconstruction	16
5.1 Principles of particle identification	16
5.2 Particle-flow algorithm	16
5.3 Primary vertex	16
5.4 Electrons	16
5.5 Muons	16
5.6 Hadronically Decayed τ Leptons	18
5.7 Jets	18
5.8 Bottom quark identification	18
5.9 Missing transverse energy	20

6 Data sets & Simulated Samples	21
6.1 Data sets	21
6.2 Event simulation	21
6.3 Backgrounds	21
6.3.1 Simulated backgrounds	21
6.3.2 Cross sections	24
7 Event Selection	25
References	26

Abstract

The Standard Model of particle physics has been very successful. But there are problems. They can be explained by new exotic particles. A search is presented for a new exotic particle. Events with jets are considered. A novel technique is used. The search is based on Run-2 proton-proton collision data at a center-of-mass energy of 13 TeV recorded with the CMS detector corresponding to an integrated luminosity of 137.1 fb^{-1} . Upper limits are set on the production cross section of a new exotic particle as a function of mass. Results are compared with theoretical predictions to obtain lower limits on the mass. At 95% confidence level, new exotic particles are excluded for masses below X GeV.

Acknowledgements

I want to thank the great people in the UZH group and at CMS Collaboration that have helped me along the way, and with whom it was a great privilege and pleasure to work on diverse projects and push the limits of our understanding of Nature.

Special thanks go to my supervisor, Prof. Dr. ...; my supervisor Dr. ...; ...

I would also like to thank my parents and family, for supporting me along my studies.

1 Introduction

² Over the last 100 years, physicists have made large strides in understanding the natural laws
³ that govern the universe as we know it. The Standard Model (SM) of particle physics describes
⁴ matter and its interactions.

⁵ In 2012, the discovery of the Higgs boson was announced by the ATLAS and CMS experiments [1–3] at CERN’s LHC. The Higgs was 47 years before that [4, 5]. Despite its many
⁶ successes, there are both theoretical and experimental reasons that imply the SM is not the final
⁷ theory of Nature.

⁸ This dissertation has the following structure: Chapter 2 discusses the SM, after which Chapter
⁹ 3 motivates the search for new hypothetical particles. Chapter 4 describes the LHC accel-
¹⁰ erator, CMS detector and the data collection. Chapter 5 describes the physics objects that are
¹¹ relevant for this thesis. After these, Chapter 7 discusses the selections.
¹²

2 The Standard Model

This chapter introduces the Standard Model (SM) of particle physics. I left a bit of text with equations, citations, figures, and tables as an example of this template.

2.1 The Standard Model

A rough timeline of the experimental discovery of particles is given by Fig. 2.1. More detailed historical discussions can be found in Refs. [6–8].

With a mass of $m_t \approx 172.8 \text{ GeV}$ [10, p. 32], the top quark is by far the heaviest fermion.

The discovery of the Higgs was announced in 2012 [1–3, 11]. A single Higgs boson is the simplest and most minimal solution, although it is possible to achieve SBB with more than one Higgs boson. No evidence of additional Higgs bosons have been found so far [12].

2.1.1 The Standard Model Lagrangian

The SM is encoded in the *SM Lagrangian density*. The terms of the Lagrangian density can be grouped into three separate *sectors*:

$$\mathcal{L}_{\text{SM}} = \mathcal{L}_{\text{gauge}} + \mathcal{L}_{\text{Higgs}} + \mathcal{L}_{\text{Yukawa}}. \quad (2.1)$$

Secondly, the SM is a *gauge theory*: It has an internal symmetry that corresponds to the local $SU(3)_C \times SU(2)_L \times U(1)_Y$ symmetry group. The SM gauge group is spontaneously broken to

$$SU(3)_C \times SU(2)_L \times U(1)_Y \xrightarrow{\text{SSB}} SU(3)_C \times U(1)_{\text{EM}} \quad (2.2)$$

by the nonzero vev of the Higgs field, where $U(1)_{\text{EM}}$ is the gauge symmetry group for QED.

2.1.2 The gauge sector

The gauge sector can be written as

$$\mathcal{L}_{\text{gauge}} = \sum_f \sum_{\psi_f} \bar{\psi}_f i\gamma^\mu D_\mu \psi_f - \frac{1}{4} G_{\mu\nu}^a G_a^{\mu\nu} - \frac{1}{4} W_{\mu\nu}^i W_i^{\mu\nu} - \frac{1}{4} B^{\mu\nu} B^{\mu\nu}, \quad (2.3)$$

in natural units $c = \hbar = 1$ [14], and where $a = 1, \dots, 8$ and $i = 1, 2, 3$. In the first term, matter is given by five fermion fields ψ_f in three generations $f = 1, 2, 3$;

$$Q_L^f = \begin{pmatrix} u_L^f \\ d_L^f \end{pmatrix}, \quad u_R^f, \quad d_R^f, \quad L_L^f = \begin{pmatrix} \nu_L^f \\ e_L^f \end{pmatrix}, \quad e_R^f. \quad (2.4)$$

Their Dirac adjoints are given by $\bar{\psi}_f = \psi_f^\dagger \gamma^0$.

The covariant derivative

$$D_\mu = \partial_\mu + ig_s t_a G_\mu^a + ig T_i W_\mu^i + ig' \frac{Y}{2} B_\mu \quad (2.5)$$

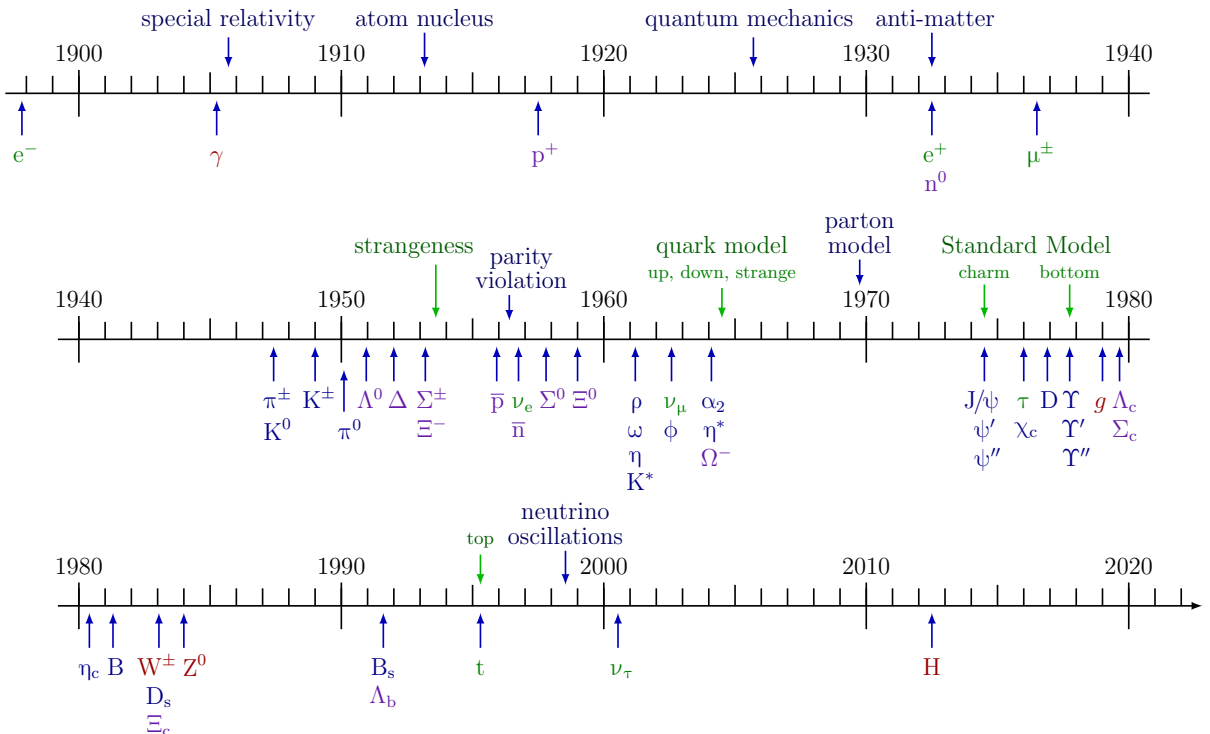


Figure 2.1: A timeline of particle physics in the last 130 years. Adapted from Ref. [9].

three generations of matter (fermions)			interactions / force carriers (bosons)		
mass charge spin	I	II	III		
	$=2.2 \text{ MeV}/c^2$ $\frac{2}{3}$ $\frac{1}{2}$ u up	$=1.28 \text{ GeV}/c^2$ $\frac{2}{3}$ $\frac{1}{2}$ c charm	$=173.1 \text{ GeV}/c^2$ $\frac{2}{3}$ $\frac{1}{2}$ t top	0 0 1 g gluon	$=124.97 \text{ GeV}/c^2$ 0 0 0 H higgs
QUARKS	$=4.7 \text{ MeV}/c^2$ $-\frac{1}{3}$ $\frac{1}{2}$ d down	$=96 \text{ MeV}/c^2$ $-\frac{1}{3}$ $\frac{1}{2}$ s strange	$=4.18 \text{ GeV}/c^2$ $-\frac{1}{3}$ $\frac{1}{2}$ b bottom	0 0 1 γ photon	SCALAR BOSONS
LEPTONS	$=0.511 \text{ MeV}/c^2$ -1 $\frac{1}{2}$ e electron	$=105.66 \text{ MeV}/c^2$ -1 $\frac{1}{2}$ μ muon	$=1.7768 \text{ GeV}/c^2$ -1 $\frac{1}{2}$ τ tau	$=91.19 \text{ GeV}/c^2$ 0 1 Z Z boson	VECTOR BOSONS
	$<1.0 \text{ eV}/c^2$ 0 $\frac{1}{2}$ ν_e electron neutrino	$<0.17 \text{ MeV}/c^2$ 0 $\frac{1}{2}$ ν_μ muon neutrino	$<18.2 \text{ MeV}/c^2$ 0 $\frac{1}{2}$ ν_τ tau neutrino	$=80.433 \text{ GeV}/c^2$ ± 1 1 W W boson	GAUGE BOSONS

Figure 2.2: A table of the particles in Standard Model of particle physics and their properties. Figure taken from Ref. [13].

Table 2.1: Summary of the representation and quantum numbers SM fields. Bold numbers indicate the dimension of the representation under the respective gauge group.

Field name	Symbol	Representations		Quantum numbers		
		SU(3) _C	SU(2) _L	T_3	$Y/2$	$Q = T_3 + Y/2$
Quark doublet	$Q_L = \begin{pmatrix} u_L \\ d_L \end{pmatrix}$	3	2	$\begin{pmatrix} +\frac{1}{2} \\ -\frac{1}{2} \end{pmatrix}$	$+\frac{1}{6}$	$\begin{pmatrix} +\frac{2}{3} \\ -\frac{1}{3} \end{pmatrix}$
Up-quark singlet	u_R	3	1	$+\frac{2}{3}$	$+\frac{2}{3}$	$+\frac{2}{3}$
Down-quark singlet	d_R	3	1	$-\frac{1}{3}$	$-\frac{1}{3}$	$-\frac{2}{3}$
Lepton doublet	$L_L = \begin{pmatrix} \nu_L \\ e_L \end{pmatrix}$	1	2	$\begin{pmatrix} +\frac{1}{2} \\ -\frac{1}{2} \end{pmatrix}$	$-\frac{1}{2}$	$\begin{pmatrix} 0 \\ -1 \end{pmatrix}$
Lepton singlet	e_R	1	1	0	-1	-1
Gluon field	G_μ^a	8	1	0	0	0
Weak gauge field	$W_\mu^i = \begin{pmatrix} W_\mu^+ \\ W_\mu^- \\ W_\mu^3 \end{pmatrix}$	1	3	$\begin{pmatrix} +1 \\ -1 \\ 0 \end{pmatrix}$	0	$\begin{pmatrix} +1 \\ -1 \\ 0 \end{pmatrix}$
Hypercharge field	B_μ	1	1	0	0	0
Higgs doublet	$\Phi = \begin{pmatrix} \phi^+ \\ \phi^0 \end{pmatrix}$	1	2	$\begin{pmatrix} +\frac{1}{2} \\ -\frac{1}{2} \end{pmatrix}$	$+\frac{1}{2}$	$\begin{pmatrix} +1 \\ 0 \end{pmatrix}$
Conjugate Higgs doublet	$\Phi^c = \begin{pmatrix} \phi^{0*} \\ \phi^- \end{pmatrix}$	1	2	$\begin{pmatrix} +\frac{1}{2} \\ -\frac{1}{2} \end{pmatrix}$	$-\frac{1}{2}$	$\begin{pmatrix} 0 \\ -1 \end{pmatrix}$

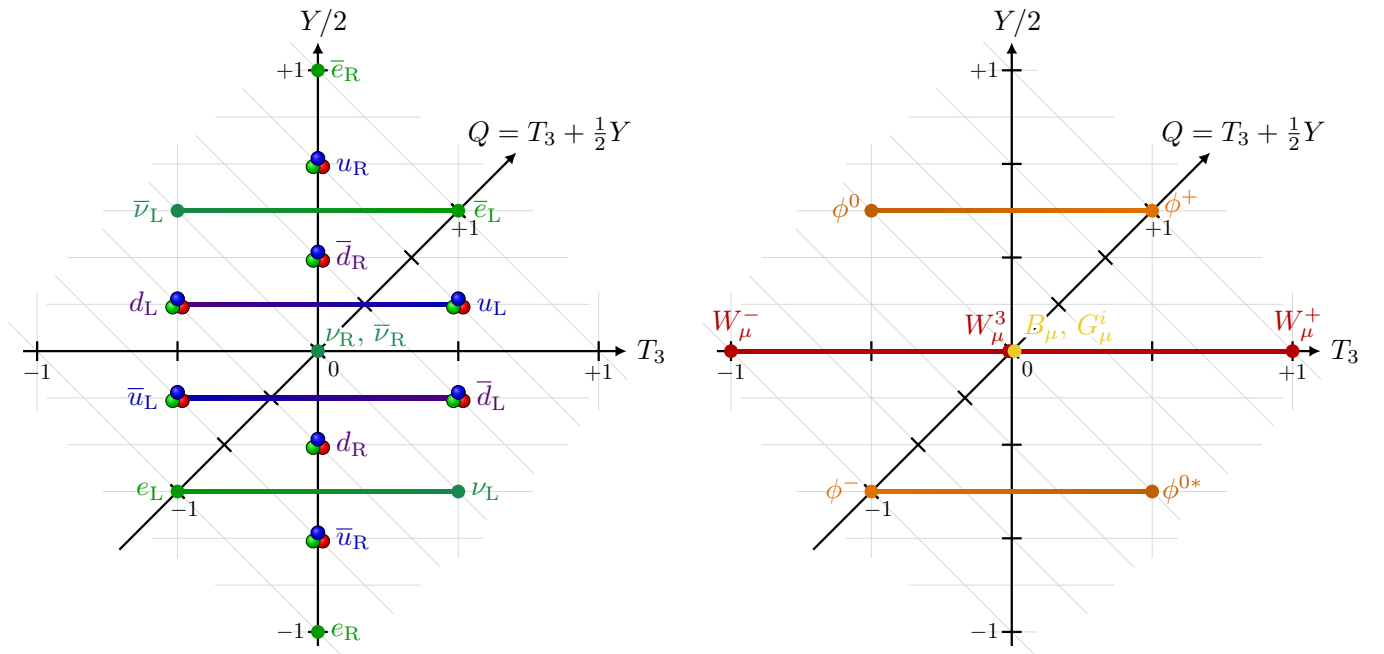


Figure 2.3: Graph of the $(T_3, Y/2)$ quantum numbers.

35 where T_i and t_a are the generators for $SU(2)_L$ and $SU(3)_C$, respectively, and Y is the weak
 36 hypercharge of the field that D_μ acts on.

37 Through the Higgs mechanism, the gauge bosons acquire mass and mix into the mass eigen-
 38 states

$$W_\mu^\pm = \frac{W_\mu^1 \mp iW_\mu^2}{\sqrt{2}}, \quad Z_\mu = W_\mu^3 \cos \theta_W + B_\mu^3 \sin \theta_W, \quad A_\mu = W_\mu^3 \sin \theta_W - B_\mu^3 \cos \theta_W, \quad (2.6)$$

39 where W_μ^\pm are the charged W boson fields, Z_μ is the neutral Z boson field, A_μ is the photon
 40 field, and θ_W is the Weinberg angle given by $\sin \theta_W = g'/\sqrt{g^2 + g'^2}$. After mixing, the new
 41 covariant derivative becomes

$$D_\mu = \partial_\mu + ig_s t_a G_\mu^a + i \frac{g}{\sqrt{2}} T^+ W_\mu^+ + i \frac{g}{\sqrt{2}} T^- W_\mu^- + i \frac{g}{\cos \theta_W} (T_3 - \sin^2 \theta_W Q) Z_\mu + ieQ A_\mu, \quad (2.7)$$

42 with ladder operators $T^\pm = T_1 \pm iT_2$.

43 2.1.3 The Yukawa sector

44 In order to explain mass of the fermions,

$$\mathcal{L}_{\text{Yukawa}} = -Y_d^{fg} \bar{Q}_L^f \Phi d_R^g - Y_u^{fg} \bar{Q}_L^f \Phi^c u_R^g - Y_e^{fg} \bar{L}_L^f \Phi e_R^g + \text{h.c.}, \quad (2.8)$$

45 with the conjugate Higgs doublet $\Phi^c = i\sigma_2 \Phi^\dagger$, and unitary Yukawa matrices Y_d^{fg} , Y_u^{fg} , $Y_e^{fg} \in$
 46 $U(3)$ that mixes the fermion generations. As Φ is a scalar field that forms a weak isospin doublet,

$$\Phi = \begin{pmatrix} \phi^+ \\ \phi^0 \end{pmatrix}. \quad (2.9)$$

47 Because the Higgs vev is nonzero, we can fix the $SU(2)_L$ gauge. It is convenient to choose
 48 the unitary gauge

$$\Phi = \frac{1}{\sqrt{2}} \begin{pmatrix} 0 \\ v + h \end{pmatrix}, \quad (2.10)$$

49 with the vev $v \approx 246$ GeV, a real constant, and the neutral Higgs field h , a (real) scalar.
 50 Therefore, after SSB, we are left with

$$\mathcal{L}_{\text{Yukawa}} = -\frac{Y_d^{fg}}{\sqrt{2}} \bar{d}_L^f (v + h) d_R^g - \frac{Y_u^{fg}}{\sqrt{2}} \bar{u}_L^f (v + h) u_R^g - \frac{Y_e^{fg}}{\sqrt{2}} \bar{e}_L^f (v + h) e_R^g + \text{h.c.} \quad (2.11)$$

51 2.1.4 CKM matrix

52 To explain the suppressed decay rate of $K^0 \rightarrow \mu^+ \mu^-$, Glashow, Iliopoulos, and Maiani used a
 53 mixing matrix and proposed the existence of the charm quark [15]. This is referred to as the
 54 *Glashow–Iliopoulos–Maiani (GIM) mechanism*. The mixing of two quark generations is given
 55 by the *Cabibbo matrix*:

$$\begin{pmatrix} d' \\ s' \end{pmatrix} = \begin{pmatrix} \cos \theta_C & \sin \theta_C \\ -\sin \theta_C & \cos \theta_C \end{pmatrix} \begin{pmatrix} d \\ s \end{pmatrix}, \quad (2.12)$$

56 where $|d'\rangle$ and $|s'\rangle$ represent the weak eigenstates, which are linear combinations of the mass
 57 eigenstates $|d\rangle$ and $|s\rangle$. The mixing is quantified with the *Cabibbo angle* $\theta_C \approx 13.04^\circ$.

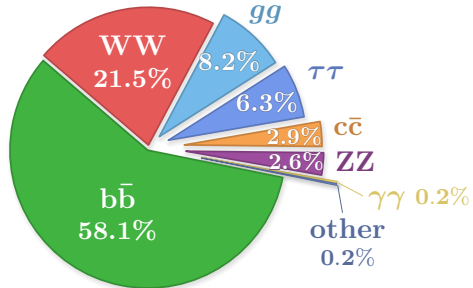


Figure 2.4: Pie chart of Higgs branching fractions.

58 The mixing of three generations is given by

$$\begin{pmatrix} d' \\ s' \\ b' \end{pmatrix} = \begin{pmatrix} V_{ud} & V_{us} & V_{ub} \\ V_{cd} & V_{cs} & V_{cb} \\ V_{td} & V_{ts} & V_{tb} \end{pmatrix} \begin{pmatrix} d \\ s \\ b \end{pmatrix}, \quad (2.13)$$

59 where the matrix is the so-called *Cabbibo-Kobayashi-Maskawa (CKM) matrix*, denoted by V_{CKM} .

60 2.2 Higgs

61 A pie chart of Higgs decay can be found in Fig. 2.4.

62 2.3 The physics of proton-proton collisions

63 The substructure of the proton has been carefully studied in deep inelastic scattering (DIS)
64 experiments at SLAC [16, 17] and DESY [18], which collided electrons or positrons with protons.

65 In the parton model, *parton distribution functions* (PDFs) describe the probability of finding
66 a parton of type p with momentum fraction x in a collision at some momentum scale Q as a
67 function of the form $f_p(x, Q^2)$ [19–23]. The proton has *valence quarks* and *sea quarks*. To reflect
68 the proton quantum numbers, the PDFs are normalized:

$$\int_0^1 [f_u(x, Q^2) - f_{\bar{u}}(x, Q^2)] dx = 2, \quad \int_0^1 [f_d(x, Q^2) - f_{\bar{d}}(x, Q^2)] dx = 1. \quad (2.14)$$

69 This follows from the factorization theorem [25, 26], which provides a formula to calculate
70 the cross sections of a hard process with an integral of the form

$$\sigma(\text{pp} \rightarrow X + Y) = \sum_{i,j} \int_0^1 \int_0^1 f_i(x_1, Q^2) f_j(x_2, Q^2) \hat{\sigma}_{ij \rightarrow X}(x_1, x_2, Q^2) dx_1 dx_2, \quad (2.15)$$

71 where $\hat{\sigma}_{ij \rightarrow X}(x_1, x_2, Q^2)$ is the parton-level cross section of the hard process, $i + j \rightarrow X$, and
72 parton i (j) carries a fraction x_1 (x_2) of the momentum of its mother proton.

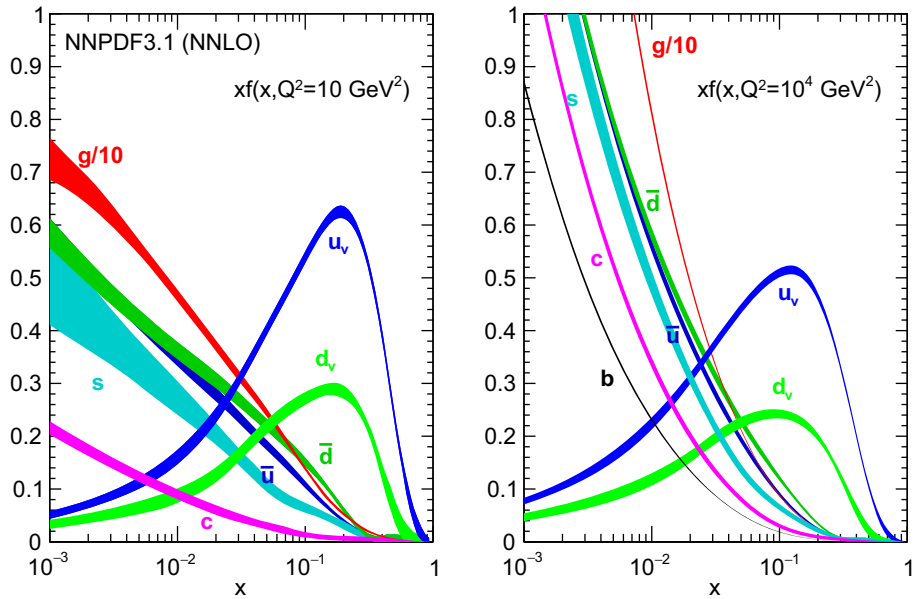


Figure 2.5: Plot of the proton PDF $f_p(x, Q^2)$ times the momentum fraction x as calculated by NNPDF3.1 at NNLO accuracy in perturbation theory for $Q^2 = 10 \text{ GeV}^2$ (left) and $Q^2 = 10^4 \text{ GeV}^2$ (right). Adapted from [24].

⁷³ **3 Beyond the Standard Model**

⁷⁴ The SM of particle physics is successful. Fine-structure constant $\alpha = e^2/4\pi$ has been precisely
⁷⁵ calculated and measured [27–30]. In 2012, the discovery of the Higgs boson was announced by
⁷⁶ the ATLAS and CMS experiments at the CERN LHC [1–3, 11], more than 47 years after its
⁷⁷ prediction [4, 5]. But there are both problems. The following section highlights several examples
⁷⁸ of open questions in physics.

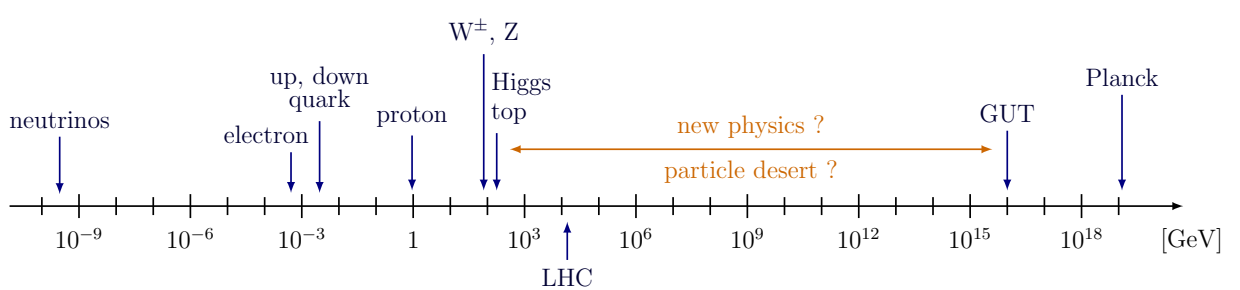


Figure 3.1: Logarithmic scale of different energy scales in particle physics. Adapted from Ref. [9].

79 4 The CMS Experiment

80 This chapter will discuss the experimental setup.

81 4.1 The Large Hadron Collider

82 The Large Hadron Collider (LHC) is the world's largest and most powerful particle collider
 83 with a 27 km circumference and a record collision energy of 13.6 TeV. It surpasses the Tevatron
 84 accelerator at Fermilab in the United States [32] (6.3 km, 1.96 TeV), and LEP (209 GeV) [10,
 85 Section 32].

86 During the data-taking period of 2015 to 2018, referred to as "Run 2", the energy of each
 87 proton beam was 6.5 TeV, which means the center-of-mass energy was $\sqrt{s} = 13$ TeV. The LHC
 88 machine is described in more technical detail in Ref. [33].

89 4.1.1 Luminosity

90 It depends on several beam parameters. The simplified expression is [10, p. 533]:

$$\mathcal{L} = \frac{N_1 N_2 f}{A}. \quad (4.1)$$

91 The LHC is designed to reach the nominal luminosity of $\mathcal{L} = 10^{34} \text{ cm}^{-2} \text{ s}^{-1}$. See Fig. 4.2. Each
 92 bunch contains about 110 billion protons [33, 35].

93 Figure 4.4 shows the distribution of the number of interactions per bunch crossing in all

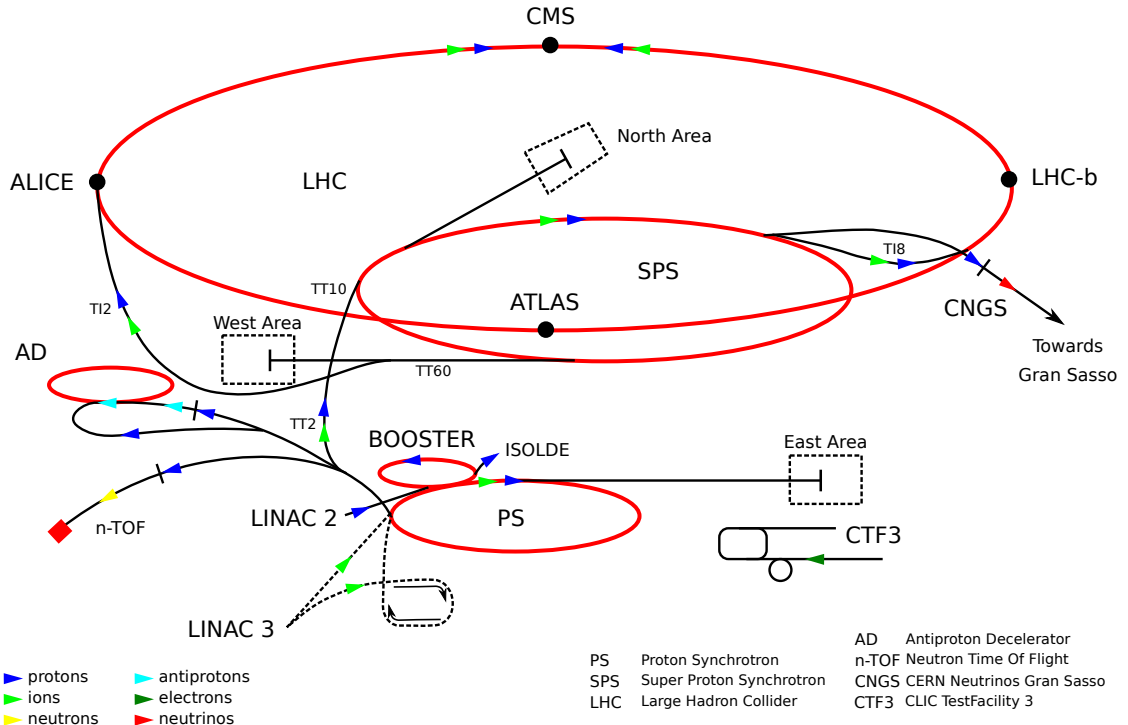


Figure 4.1: CERN's accelerator complex. Taken from [31].

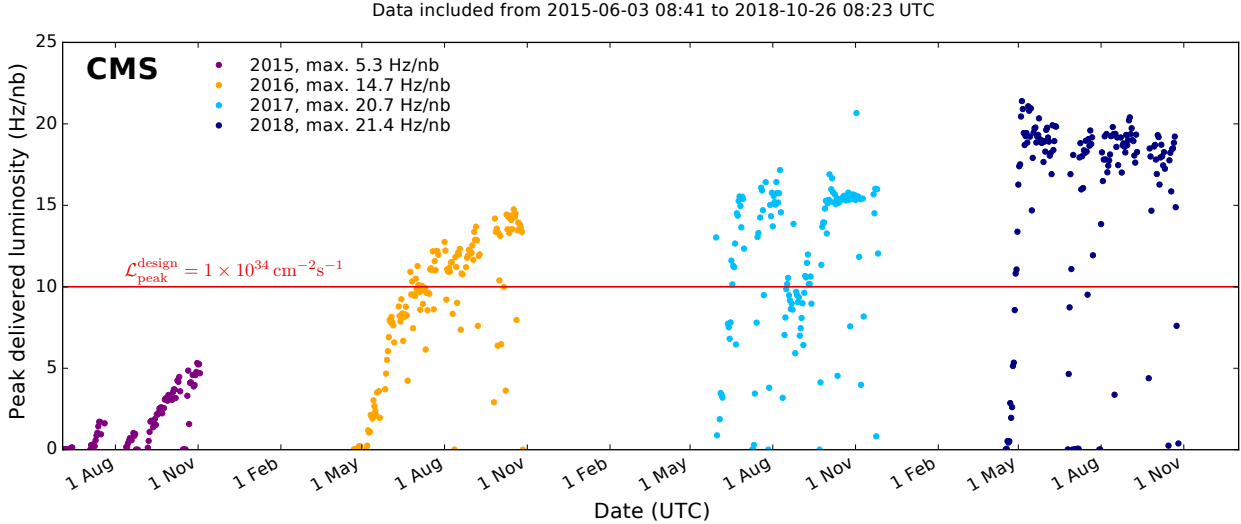


Figure 4.2: The instantaneous luminosity \mathcal{L} . The design luminosity is $\mathcal{L}_{\text{peak}}^{\text{design}} = 10^{34} \text{ cm}^{-2} \text{s}^{-1}$. Adapted from [34].

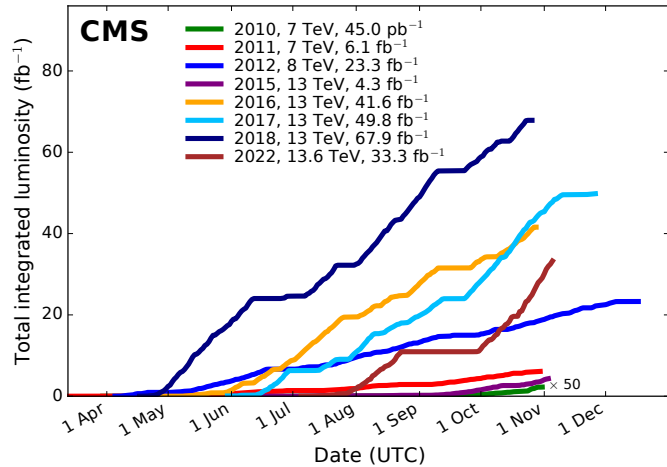


Figure 4.3: Integrated luminosity collected by CMS at $\sqrt{s} = 13 \text{ TeV}$. Figure taken from [34].

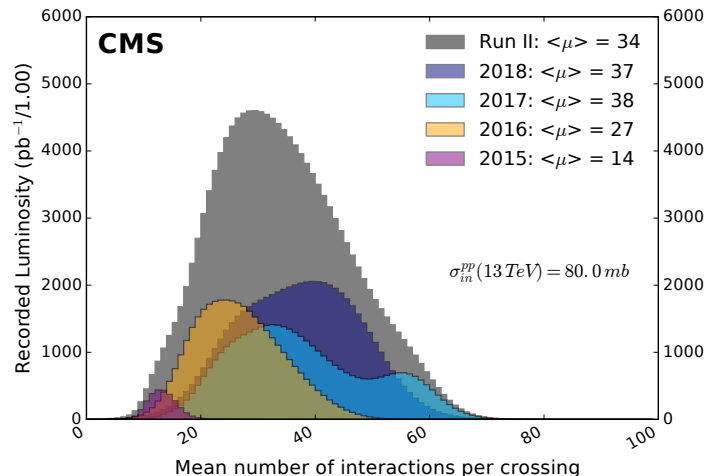


Figure 4.4: Distribution of number of pp interactions, assuming an inelastic cross section of 80 mb. Figure taken from [34].

94 data-taking years of Run 2.

95 Figure 4.3 shows the data of each data-taking year with *integrated luminosity* L , which is

$$L := \int_{\text{data taking}} \mathcal{L}(t) dt, \quad (4.2)$$

96 given in units of inverse area, such as the inverse barn (b^{-1}). Between 2016 and 2018, CMS
97 collected about 138 fb^{-1} of pp collision data for physics analysis.

98 4.2 The CMS detector

99 The Compact Muon Solenoid (CMS) detector at one of the interaction points at the LHC. An
100 illustration is shown in Fig. 4.5. A detailed description can be found in Ref. [36].

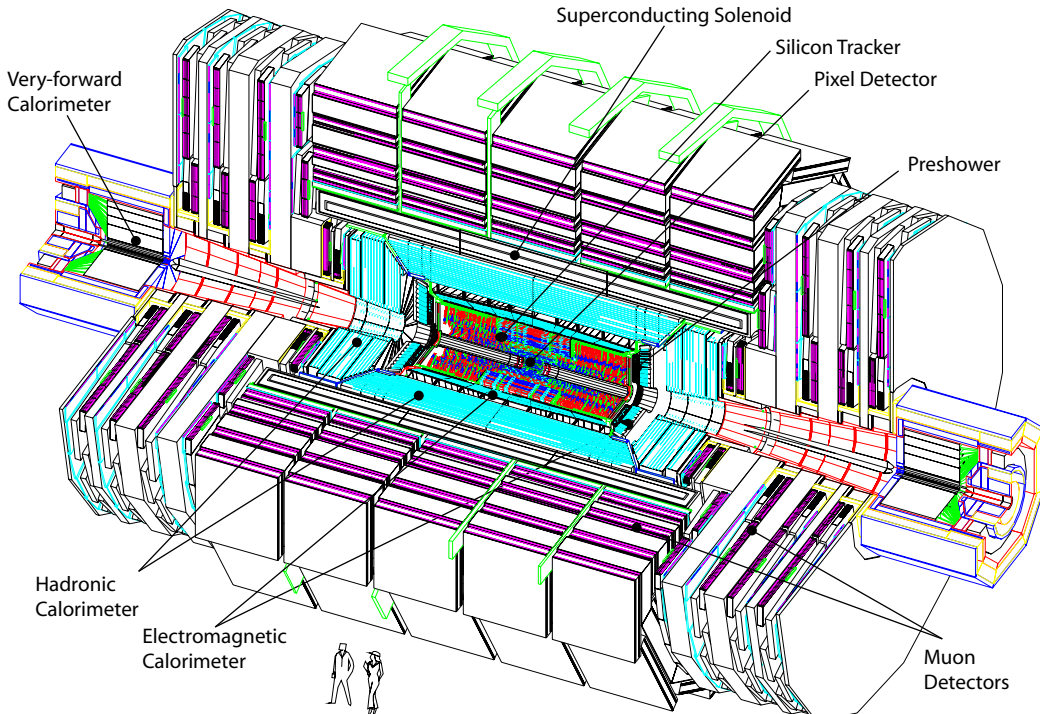


Figure 4.5: The CMS detector. Taken from [36].

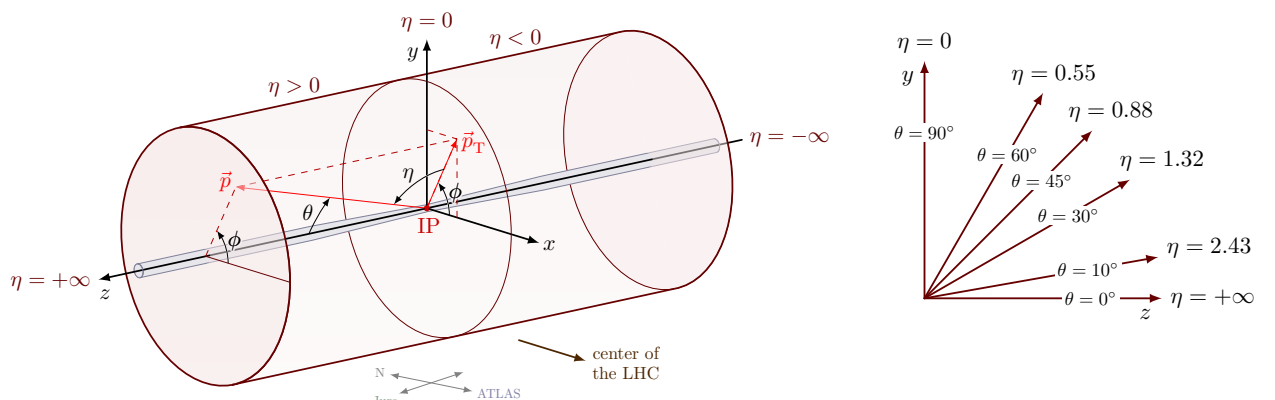


Figure 4.6: Left: The conventional coordinate system of CMS with momentum vector \vec{p} . Taken from [37]. Right: Pseudorapidity. Taken from [38].

101 **4.2.1 Coordinate system**

102 The conventional coordinate system of CMS is defined in Fig. 4.6.

103 **4.2.2 The solenoid magnet & flux-return yoke**

104 The superconducting solenoid magnet is a 13 m long cylinder with an inner diameter of 6 m. The
105 yoke [42].

106 **4.2.3 The pixel tracker**

107 The inner tracker system has a *silicon pixel tracker* and a *silicon microstrip tracker*. Figure 4.8
108 presents a closer look of the full tracker layout. The pixel tracker from 2008 up to 2016 was
109 composed of 1440 sensor modules with a total of 66 million silicon pixels [43]. During the
110 technical shutdown it was upgraded with 1856 modules with 124 million pixels in total [41, 44].
111 Their layouts are compared in Fig. 4.9. See Refs. [43, 45] for more information on the resolution.

112 **4.2.4 The silicon strip tracker**

113 The silicon strip tracker is larger. A detailed description of the tracking and vertexing software
114 is given in Ref. [43].

115 **4.2.5 The electromagnetic calorimeter**

116 The *electromagnetic calorimeter* (ECAL) is built around the tracker. The energy resolution can
117 be parametrized as a function of energy [36]:

$$\left(\frac{\sigma_E}{E}\right)^2 = \left(\frac{S}{\sqrt{E}}\right)^2 \oplus \left(\frac{N}{E}\right)^2 \oplus C^2, \quad (4.3)$$

118 with the stochastic term S , the noise N , and a constant term C . The technical design report [46]
119 describes the ECAL in more technical detail.

120 **4.2.6 The hadronic calorimeter**

121 The last subdetector inside the solenoid is the *hadron calorimeter* (HCAL). The jet energy
122 resolution can be found in Ref. [47]

123 The *very forward HCAL* (HF) is positioned around the beamline outside the detector.

124 **4.2.7 The muon system**

125 The muon system is outside the solenoid magnet. The final momentum resolution can be roughly
126 parametrized as follows:

$$\left(\frac{\sigma_{p_T}}{p_T}\right)^2 = (A \cdot p_T)^2 \oplus C^2, \quad (4.4)$$

127 where A , and C are constants determined by the hit resolution and multiple scattering, respec-
128 tively [48]. The resolution grows with momentum, because the track becomes more straight,
129 which increases the uncertainty in its curvature. The technical design report can be found in
130 Ref. [49].

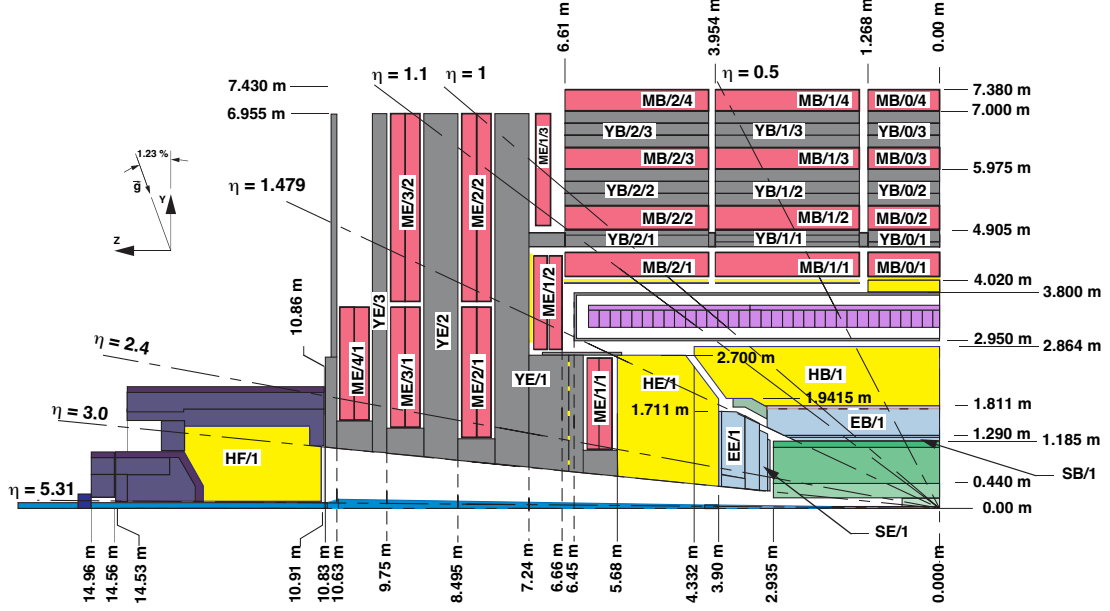


Figure 4.7: Schematic of one quadrant of the CMS detector in the positive zy -plane. Adapted from [39].

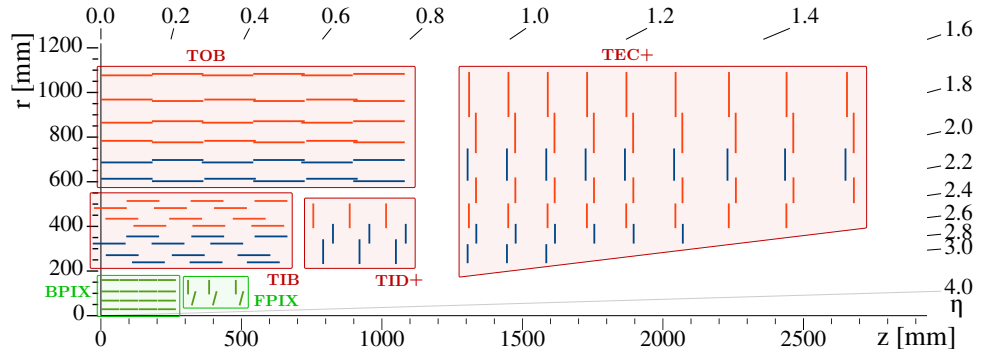


Figure 4.8: Schematic view of the CMS tracking system. Adapted from [40].

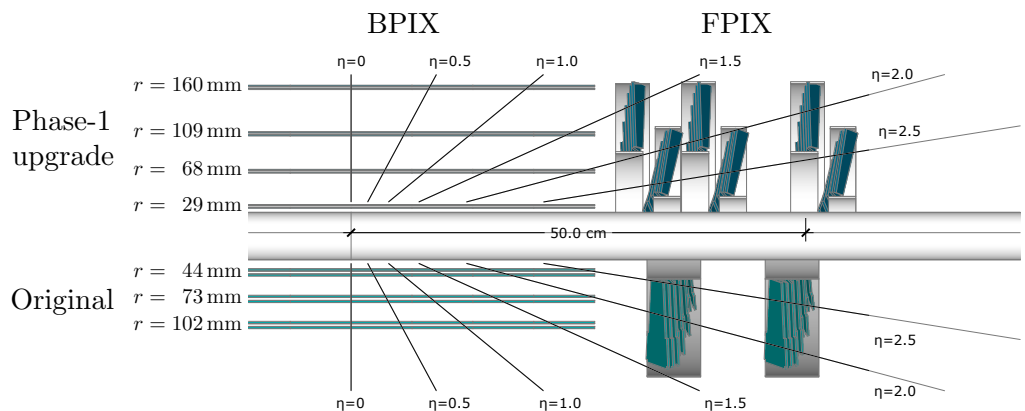


Figure 4.9: Layout of the CMS pixel detector. Adapted from [41].

¹³¹ **4.2.8 The trigger system**

¹³² The collision rate of 40 MHz is higher than is possible to record offline. The *L1 trigger* has a
¹³³ rate of about 100 kHz. The next level, is the *high-level trigger* (HLT). See Ref. [50].

5 Object & Event Reconstruction

134 This chapter explains object and event reconstruction in the CMS experiment.

5.1 Principles of particle identification

137 Figure 5.1 compares the lifetime, dividing them in different regions of stability in the context of
138 the CMS experiment.

139 Each of these particles has a unique set of properties that leave a characteristic signal in one
140 or more of the subdetector, as illustrated in Fig. 5.2.

5.2 Particle-flow algorithm

142 The particle-flow (PF) algorithm [53, 54] fully reconstructs the event of a pp collision with an
143 optimized combination of all measurements of the CMS subsystems.

144 Tracks in the inner tracker or muon system are iteratively built from hits, using the *Kalman-*
145 *filter (KF) technique* [55, 56].

5.3 Primary vertex

147 The algorithm locates primary vertices (PVs) of pp collisions. The tracks are clustered using the
148 *deterministic annealing algorithm* [57]. Finally, candidate vertices are fitted using an *adaptive*
149 *vertex fitter* [58]. The PV with the largest sum of momenta is assumed to be the vertex of the
150 hard scattering process [43, 54, 59].

5.4 Electrons

152 Electrons are reconstructed by associating a track in the inner tracker to clusters of energy
153 deposits in the ECAL. Candidate tracks are refitted with the *Gaussian sum filter* (GSF) [60].
154 The ECAL clusters are recombined into a so-called *supercluster*. The resolution is documented
155 in Ref. [61, 62].

156 The reconstruction and identification of electrons, as well as high-energy photons, are dis-
157 cussed in more detail in Refs. [63] and [61].

158 The *relative isolation* for electrons is computed with the so-called *rho-effective-area method* [64]:

$$I_{\text{rel}}^e := \frac{\sum_{\text{charged}} p_T + \max(0, \sum_{\text{neutral}} E_T - \rho A_{\text{eff}})}{p_T^e}. \quad (5.1)$$

5.5 Muons

160 Muon candidates in CMS are reconstructed as *standalone muons*, *tracker muons*, and/or *global*
161 *muons* [65].

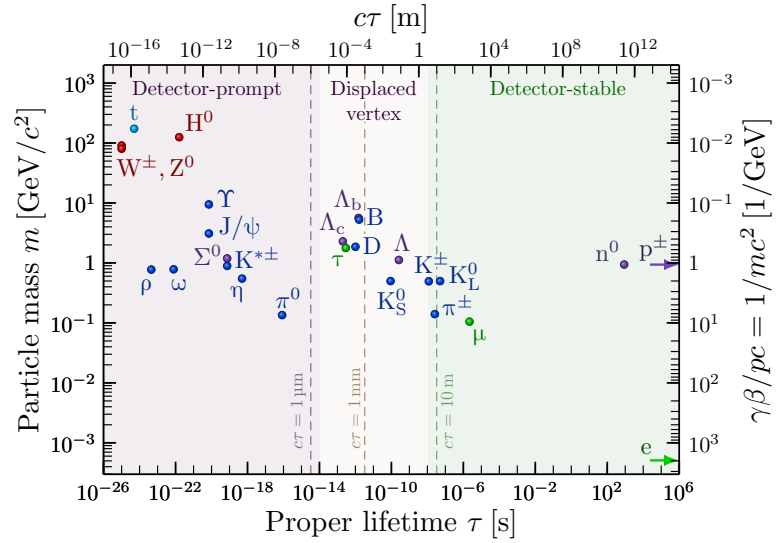


Figure 5.1: Plot of the mass versus lifetime τ of many composite and fundamental SM particles. The decay length is given by $L = \gamma\beta c\tau$, with $\gamma\beta = p/mc$. Adapted from [51].

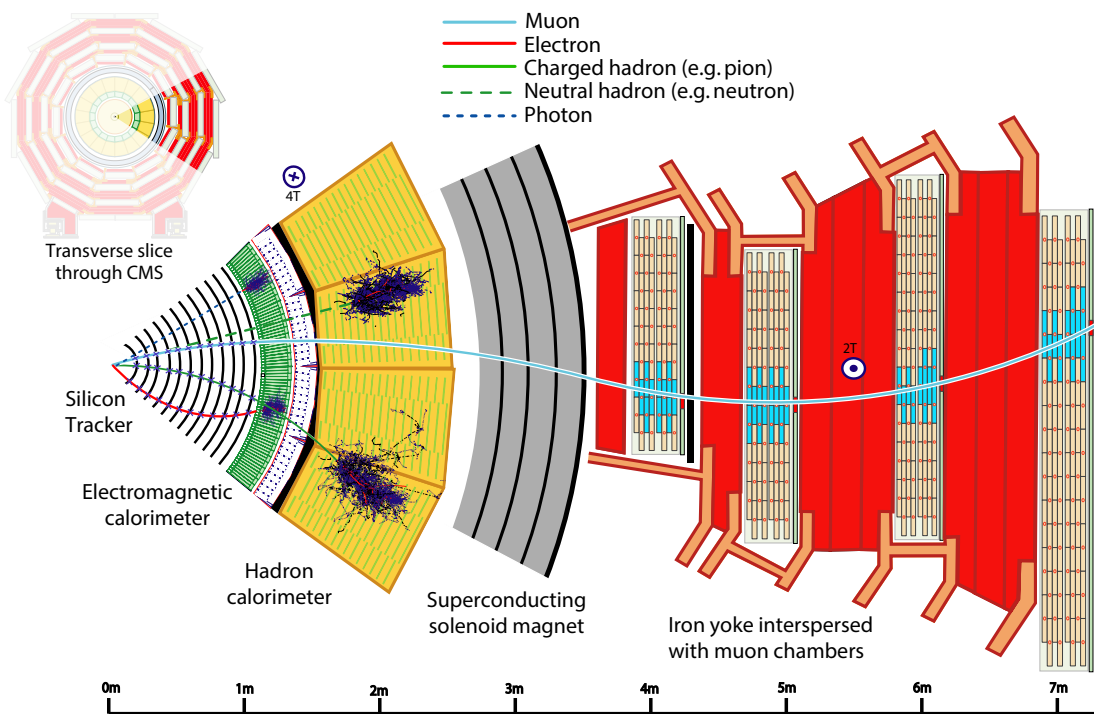


Figure 5.2: Particles in the CMS detector. Adapted from from [52].

162 The relative isolation of a muon is defined with the so-called $\Delta\beta$ -*corrections*:

$$I_{\text{rel}}^{\mu} := \frac{\sum_{\text{charged}} p_{\text{T}} + \max(0, \sum_{\text{neutral}} E_{\text{T}} - \Delta\beta \sum_{\text{charged, PU}} p_{\text{T}})}{p_{\text{T}}^{\mu}}. \quad (5.2)$$

163 5.6 Hadronically Decayed τ Leptons

164 Hadronic decays of τ leptons (τ_h) are reconstructed with the *hadron-plus-strips* (HPS) *algorithm*
165 [66–69]. About 65% of hadronic τ decays involve neutral pions, which decay promptly ($\tau =$
166 8.4×10^{-17} s) to two photons 98.8% of the time [10, p. 33].

167 The τ_h identification algorithm DEEPTAU [69] was used to discriminate against jets that are
168 initiated by quarks and gluons, as well as electrons and muons, see Fig. 5.5.

169 5.7 Jets

170 Jets are reconstructed with a clustering algorithm. The jet properties must be *infrared safe* and
171 *collinear safe*. The *anti- k_T* (AK) *algorithm* utilizes the metric

$$d_{ij} = \min(p_{\text{T},i}^{-2}, p_{\text{T},j}^{-2}) \frac{\Delta R_{ij}^2}{\Delta R_y^2}, \quad (5.3)$$

172 where $\Delta R_y = \sqrt{\Delta y^2 + \Delta\phi^2}$ is the distance in (y, ϕ) -space with the *rapidity*

$$y := \frac{1}{2} \ln \left(\frac{E + p_z}{E - p_z} \right). \quad (5.4)$$

173 If a cluster i of combined objects satisfies

$$d_{ij} > d_{iB} = p_{\text{T},i}^{-2}, \quad (5.5)$$

174 More info is given in Ref. [54, 71]. The AK algorithm is implemented in the FASTJET library [72,
175 73], and *charged-hadron subtraction* (CHS) is used.

176 The CMS Collaboration determines *jet energy corrections* (JECs) in several steps, which are
177 explained in detail in Ref. [74]. Additionally, the jet energy and *jet energy resolution* (JER) of
178 jets in simulation are corrected to obtain better agreement between simulation and data.

179 Genuine jets are distinguished from pileup jets with the identification algorithm [75]. Iden-
180 tification [76] removes spurious jet-like features that originate from isolated noise patterns in
181 certain HCAL regions.

182 5.8 Bottom quark identification

183 The DEEPCSV algorithm [77, 78] for b tagging jets. DEEPCSV is a deep neural network
184 (DNN) with four hidden layers that is an extension of the combined secondary vertex (CSV)
185 algorithm [77, 78].

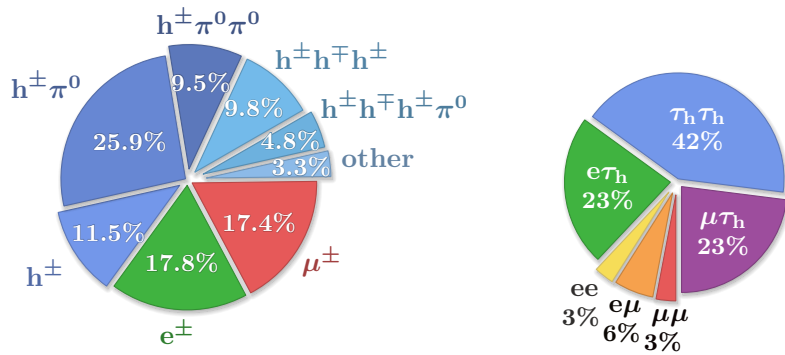


Figure 5.3: Pie charts of branching fractions. **Left:** τ lepton decay. **Right:** Decay channels of a pair of τ leptons. Numbers from PDG [10, p. 28].

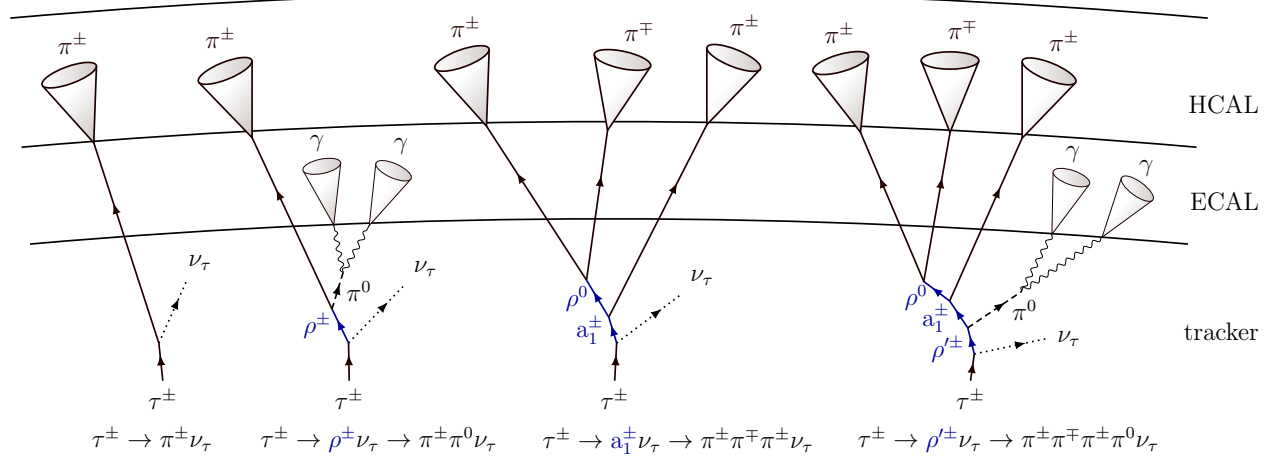


Figure 5.4: An illustration τ_h signatures. Inspired by Ref. [70, p. 37].

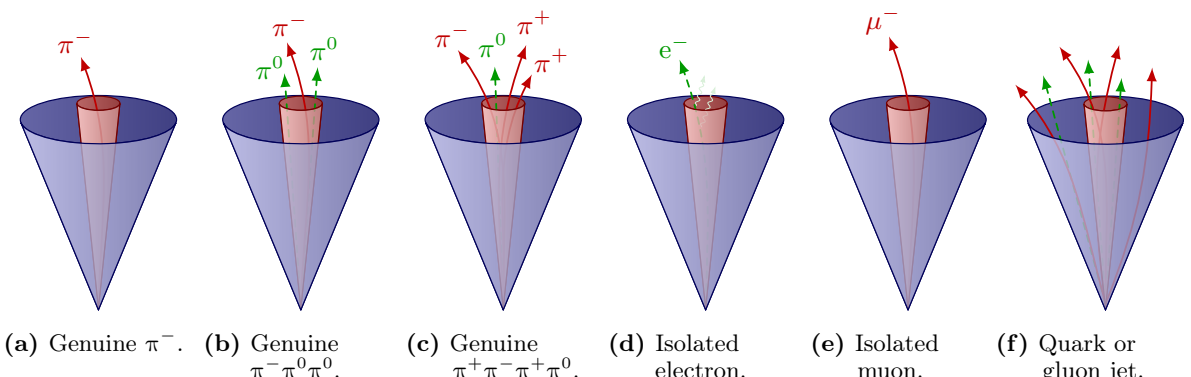


Figure 5.5: Illustration of several hadronic decay modes of the τ leptons (a-c) and their backgrounds (d-f).

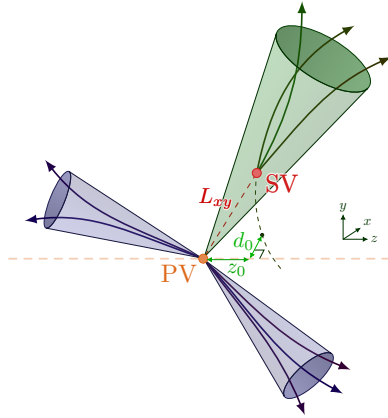


Figure 5.6: B-tagging.

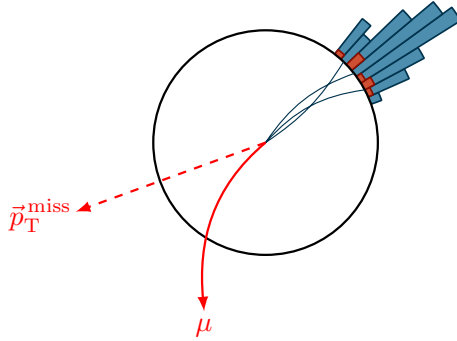


Figure 5.7: Illustration of missing transverse energy (MET) with a muon track (red), and energy deposits in the calorimeters.

186 **5.9 Missing transverse energy**

187 The vectorially sum of all particles gives the missing momentum

$$\vec{p}_T^{\text{miss}} = - \sum_i \vec{p}_T^i. \quad (5.6)$$

188 This vector, or its length, is often referred to as the *missing transverse momentum*, or *missing
189 transverse energy* (MET). Several corrections are applied [54]. More details can be found in
190 Refs. [79] and [80].

191 6 Data sets & Simulated Samples

192 This chapter will discuss in more detail the data sets of pp collision events used, as well as the
193 samples of simulated background events.

194 6.1 Data sets

195 The total data set recorded between 2016 and 2018 corresponds to an integrated luminosity of
196 approximately 138 fb^{-1} at $\sqrt{s} = 13 \text{ TeV}$. The run ranges and integrated luminosity per year are
197 listed in Table 6.1.

Table 6.1: LHC run number ranges and integrated luminosity L .

Run number range	$L [\text{fb}^{-1}]$
272007–284044	36.3
297020–306462	41.5
315252–325175	59.7

198 6.2 Event simulation

199 The PYTHIA parameters affecting the description of the underlying event are set to the CUETP8M1
200 (CP5) tune for all 2016 (2017 and 2018) samples [82, 83], except for the 2016 $t\bar{t}$ sample, for
201 which CUETP8M2T4 [84] is used. The interaction with the CMS detector is simulated by
202 GEANT4 [85]. Pileup is generated with PYTHIA. Event generation is described in more detail in
203 Refs. [10, p. 717], [86] and [87].

204 6.3 Backgrounds

205 6.3.1 Simulated backgrounds

206 All the simulated background samples used in this thesis are listed in Table 6.2. The $W + \text{jets}$ and
207 $Z + \text{jets}$ processes are generated with MADGRAPH [88] at LO precision. The MLM jet matching
208 and merging scheme [89] is used to match partons between MADGRAPH and PYTHIA and prevent
209 overcounting. The $Z + \text{jets}$ samples generated at NLO by MADGRAPH5_aMC@NLO [90]. The
210 production of $t\bar{t}$ and singly produced top quarks is simulated with the POWHEG [91–93] 2.0 and
211 1.0 generators, respectively, at NLO precision [94–97]. Diboson production is generated at LO
212 with PYTHIA 8 [98, 99]. The NNPDF3.0 PDF sets [100] are used for 2016. The NNPDF3.1
213 PDF [24] sets are used for 2017 and 2018 samples.

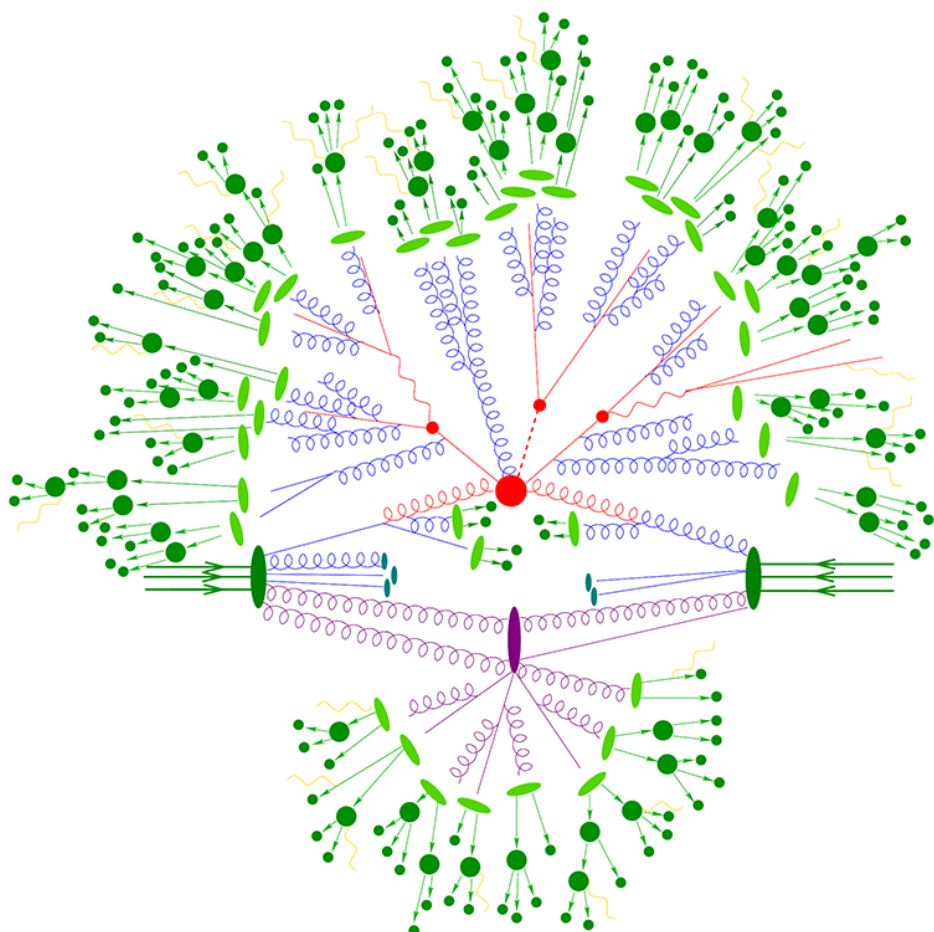


Figure 6.1: Schematic diagram explaining event generation of two colliding protons. Retrieved from [81].

Table 6.2: Summary of simulated SM backgrounds

Process	Generators	Cross section σ [pb]
Drell-Yan, $Z/\gamma^* \rightarrow \ell^+\ell^-$, LO		
+ jets, $10 < m_{\ell\ell} < 50$ GeV	MADGRAPH, PYTHIA	15810.0 (LO), 18610.0 (NLO)
+ jets, $m_{\ell\ell} > 50$ GeV	MADGRAPH, PYTHIA	5343.0 (LO), 6077.2 (NNLO)
+ 1 jets, $m_{\ell\ell} > 50$ GeV	MADGRAPH, PYTHIA	877.8 (LO)
+ 2 jets, $m_{\ell\ell} > 50$ GeV	MADGRAPH, PYTHIA	304.4 (LO)
+ 3 jets, $m_{\ell\ell} > 50$ GeV	MADGRAPH, PYTHIA	111.5 (LO)
+ 4 jets, $m_{\ell\ell} > 50$ GeV	MADGRAPH, PYTHIA	44.05 (LO)
Drell-Yan, $Z/\gamma^* \rightarrow \ell^+\ell^-$, NLO		
+ jets, $m_{\ell\ell} \in [100, 200]$ GeV	aMC@NLO, PYTHIA	247.8 (NLO)
+ jets, $m_{\ell\ell} \in [200, 400]$ GeV	aMC@NLO, PYTHIA	8.502 (NLO)
+ jets, $m_{\ell\ell} \in [400, 500]$ GeV	aMC@NLO, PYTHIA	0.4514 (NLO)
+ jets, $m_{\ell\ell} \in [500, 700]$ GeV	aMC@NLO, PYTHIA	0.2558 (NLO)
+ jets, $m_{\ell\ell} \in [700, 800]$ GeV	aMC@NLO, PYTHIA	0.04023 (NLO)
+ jets, $m_{\ell\ell} \in [800, 1000]$ GeV	aMC@NLO, PYTHIA	0.03406 (NLO)
+ jets, $m_{\ell\ell} \in [1000, 1500]$ GeV	aMC@NLO, PYTHIA	0.01828 (NLO)
+ jets, $m_{\ell\ell} \in [1500, 2000]$ GeV	aMC@NLO, PYTHIA	0.002367 (NLO)
+ jets, $m_{\ell\ell} \in [2000, 3000]$ GeV	aMC@NLO, PYTHIA	5.409×10^{-4} (NLO)
+ jets, $m_{\ell\ell} \in [3000, \infty]$ GeV	aMC@NLO, PYTHIA	3.048×10^{-5} (NLO)
W + jets, $W \rightarrow \ell\nu$		
+ jets	MADGRAPH, PYTHIA	52940.0 (LO), 61526.7 (NLO)
+ 1 jets	MADGRAPH, PYTHIA	8104.0 (LO)
+ 2 jets	MADGRAPH, PYTHIA	2793.0 (LO)
+ 3 jets	MADGRAPH, PYTHIA	992.5 (LO)
+ 4 jets	MADGRAPH, PYTHIA	544.3 (LO)
t̄t + jets		833.9 (NNLO)
Fully leptonic	POWHEG, PYTHIA	88.29 (NNLO), $\mathcal{B} = 10.6\%$
Semi-leptonic	POWHEG, PYTHIA	365.35 (NNLO), $\mathcal{B} = 43.9\%$
Fully Hadronic	POWHEG, PYTHIA	377.96 (NNLO), $\mathcal{B} = 45.4\%$
Single top		
t + W ⁻	POWHEG, PYTHIA	35.85 (NNLO)
̄t + W ⁺	POWHEG, PYTHIA	35.85 (NNLO)
Single t, t channel	POWHEG, PYTHIA	136.02 (NNLO)
Single ̄t, t channel	POWHEG, PYTHIA	80.95 (NNLO)
Diboson		
WW	PYTHIA	75.88 (LO)
WZ	PYTHIA	27.60 (LO)
ZZ	PYTHIA	12.14 (LO)

214 **6.3.2 Cross sections**

215 Table 6.2 also lists the theoretical cross sections σ for each sample. The events are weighted by

$$Z = \frac{L\sigma}{N_{\text{tot}}}, \quad (6.1)$$

216 or with generator weight w_{gen} ,

$$Z = \frac{L\sigma}{\sum w_{\text{gen}}} w_{\text{gen}}. \quad (6.2)$$

217 The LO cross sections of the Z + jets and W + jets samples in Table 6.2 are computed with
218 MADGRAPH. The Z + jets cross section is computed with FEWZ [101] program at NNLO in per-
219 turbative QCD, and with NLO electroweak corrections. The tt} + jets cross section was computed
220 with the TOP++v2.0 program [102, 103] at NNLO and at next-to-next-to-leading logarithmic
221 (NNLL) accuracy. The W + jets production is normalized with cross sections computed at NLO
222 accuracy.

7 Event Selection

This chapter will discuss in more detail the data sets of pp collision events used, as well as the samples of simulated background events.

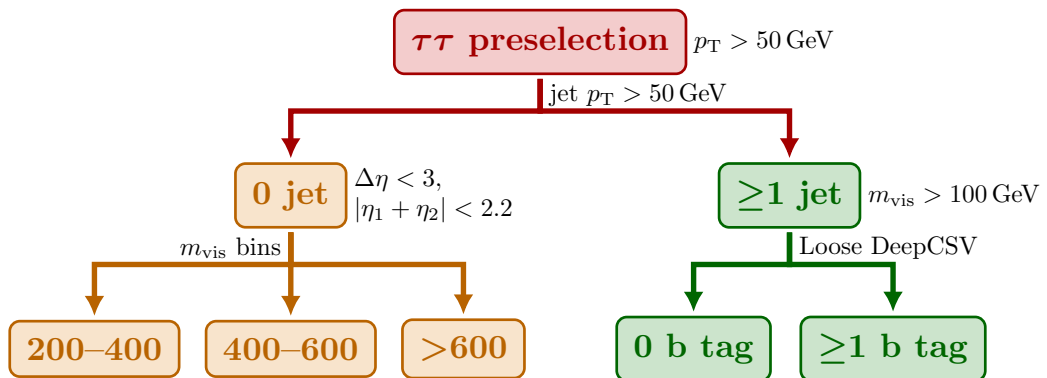


Figure 7.1: Flow chart of event selection.

226 References

- 227 [1] CMS Collaboration, “Observation of a new boson at a mass of 125 GeV with the CMS
228 experiment at the LHC”, *Phys. Lett. B* **716** (2012) 30,
229 doi:10.1016/j.physletb.2012.08.021, arXiv:1207.7235.
- 230 [2] ATLAS Collaboration, “Observation of a new particle in the search for the Standard
231 Model Higgs boson with the ATLAS detector at the LHC”, *Phys. Lett. B* **716** (2012) 1,
232 doi:10.1016/j.physletb.2012.08.020, arXiv:1207.7214.
- 233 [3] CMS Collaboration, “Observation of a new boson with mass near 125 GeV in pp
234 collisions at $\sqrt{s} = 7$ and 8 TeV”, *JHEP* **06** (2013) 081,
235 doi:10.1007/JHEP06(2013)081, arXiv:1303.4571.
- 236 [4] F. Englert and R. Brout, “Broken Symmetry and the Mass of Gauge Vector Mesons”,
237 *Phys. Rev. Lett.* **13** (1964) 321, doi:10.1103/PhysRevLett.13.321.
- 238 [5] P. W. Higgs, “Broken Symmetries and the Masses of Gauge Bosons”, *Phys. Rev. Lett.*
239 **13** (1964) 508, doi:10.1103/PhysRevLett.13.508.
- 240 [6] L. M. Brown, M. Dresden, L. H. Hoddeson, and M. West, eds., “Proceedings, 2nd
241 International Symposium on on the History of Particle Physics in the 1950s: Pions to
242 Quarks: Batavia, USA, May 1-4, 1985”. Univ. Pr., Cambridge, UK, (1989).
- 243 [7] L. H. Hoddeson, L. Brown, M. Riordan, and M. Dresden, eds., “The Rise of the standard
244 model: Particle physics in the 1960s and 1970s. Proceedings, Conference, Stanford, USA,
245 June 24-27, 1992”. (1997).
- 246 [8] D. Griffiths, “Introduction to Elementary Particles”. Wiley-VCH, 2 edition, 2008.
247 ISBN 978-3-527-40601-2.
- 248 [9] Neutelings, Izaak, “History timeline and energy scales – TikZ.net”,
249 <https://tikz.net/timeline/>, 2022. (Retrieved March 26, 2022).
- 250 [10] Particle Data Group, “Review of Particle Physics”, *PTEP* **2022** (2022) 083C01,
251 doi:10.1093/ptep/ptac097.
- 252 [11] ATLAS and CMS Collaborations, “Combined Measurement of the Higgs Boson Mass in
253 pp Collisions at $\sqrt{s} = 7$ and 8 TeV with the ATLAS and CMS Experiments”, *Phys. Rev.*
254 *Lett.* **114** (2015) 114, doi:10.1103/PhysRevLett.114.191803, arXiv:1503.07589.
- 255 [12] A. Ferrari and N. Rompotis, “Exploration of Extended Higgs Sectors with Run-2
256 Proton–Proton Collision Data at the LHC”, *Symmetry* **13** (2021), no. 11, 2144,
257 doi:10.3390/sym14081546. [Erratum: Symmetry 14, 1546 (2022)].
- 258 [13] Wikimedia Commons, “File:Standard Model of Elementary Particles.svg — Wikimedia
259 Commons, the free media repository”, https://commons.wikimedia.org/wiki/File:Standard_Model_of_Elementary_Particles.svg, 2023. (Retrieved Jan 13, 2023).
- 261 [14] G. Isidori, “Lectures notes on Flavour physics”,

- 262 <https://www.physik.uzh.ch/en/groups/isidori/teaching.html>, 2016. (Retrieved
 263 Nov 16, 2022).
- 264 [15] S. L. Glashow, J. Iliopoulos, and L. Maiani, “Weak Interactions with Lepton-Hadron
 265 Symmetry”, *Phys. Rev. D* **2** (1970) 1285, doi:10.1103/PhysRevD.2.1285.
- 266 [16] E. D. Bloom et al., “High-Energy Inelastic e^-p Scattering at 6° and 10° ”, *Phys. Rev.*
 267 *Lett.* **23** (1969) 930, doi:10.1103/PhysRevLett.23.930.
- 268 [17] M. Breidenbach et al., “Observed Behavior of Highly Inelastic Electron-Proton
 269 Scattering”, *Phys. Rev. Lett.* **23** (1969) 935, doi:10.1103/PhysRevLett.23.935.
- 270 [18] **ZEUS** and **H1** Collaborations, “Combination of measurements of inclusive deep inelastic
 271 $e^\pm p$ scattering cross sections and QCD analysis of HERA data”, *Eur. Phys. J. C* **75**
 272 (2015), no. 12, 580, doi:10.1140/epjc/s10052-015-3710-4, arXiv:1506.06042.
- 273 [19] R. P. Feynman, “The Behavior of Hadron Collisions at Extreme Energies”, in *High*
 274 *Energy Collisions: Third International Conference*, p. 237. Stony Brook, N.Y., U.S.A.,
 275 1969.
- 276 [20] J. D. Bjorken and E. A. Paschos, “Inelastic Electron-Proton and γ -Proton Scattering and
 277 the Structure of the Nucleon”, *Phys. Rev.* **185** (1969) 1975,
 278 doi:10.1103/PhysRev.185.1975.
- 279 [21] J. M. Campbell, J. W. Huston, and W. J. Stirling, “Hard Interactions of Quarks and
 280 Gluons: A Primer for LHC Physics”, *Rept. Prog. Phys.* **70** (2007) 89,
 281 doi:10.1088/0034-4885/70/1/R02, arXiv:hep-ph/0611148.
- 282 [22] R. Placakyte, “Parton Distribution Functions”, in *Proceedings, 31st International*
 283 *Conference on Physics in collisions (PIC 2011)*. Vancouver, Canada, 2011.
 284 arXiv:1111.5452.
- 285 [23] **ALICE** Collaboration, “Parton distributions for the LHC”, *Eur. Phys. J. C* **63** (2009)
 286 189, doi:10.1140/epjc/s10052-009-1072-5, arXiv:0901.0002.
- 287 [24] **NNPDF** Collaboration, “Parton distributions from high-precision collider data”, *Eur.*
 288 *Phys. J. C* **77** (2017), no. 10, 663, doi:10.1140/epjc/s10052-017-5199-5,
 289 arXiv:1706.00428.
- 290 [25] J. C. Collins and D. E. Soper, “The Theorems of Perturbative QCD”, *Ann. Rev. Nucl.*
 291 *Part. Sci.* **37** (1987) 383, doi:10.1146/annurev.ns.37.120187.002123.
- 292 [26] J. C. Collins, D. E. Soper, and G. F. Sterman, “Factorization of Hard Processes in
 293 QCD”, *Adv. Ser. Direct. High Energy Phys.* **5** (1989) 11,
 294 doi:10.1142/9789814503266_0001, arXiv:hep-ph/0409313.
- 295 [27] T. Aoyama, M. Hayakawa, T. Kinoshita, and M. Nio, “Tenth-Order QED Contribution
 296 to the Electron g-2 and an Improved Value of the Fine Structure Constant”, *Phys. Rev.*
 297 *Lett.* **109** (2012) 111807, doi:10.1103/PhysRevLett.109.111807, arXiv:1205.5368.
- 298 [28] T. Aoyama, M. Hayakawa, T. Kinoshita, and M. Nio, “Tenth-Order Electron Anomalous
 299 Magnetic Moment — Contribution of Diagrams without Closed Lepton Loops”, *Phys.*
 300 *Rev. D* **91** (2015), no. 3, 033006,
 301 doi:10.1103/PhysRevD.91.033006, 10.1103/PhysRevD.96.019901, arXiv:1412.8284.
 302 [Erratum: *Phys. Rev. D* 96, no. 1, 019901 (2017)].

- 303 [29] M. Nio, “QED tenth-order contribution to the electron anomalous magnetic moment and
304 a new value of the fine-structure constant”, Fundamental Constants Meeting, Eltville,
305 Germany, 2015. <http://www.bipm.org/cc/CODATA-TGFC/Allowed/2015-02/Nio.pdf>.
- 306 [30] D. Hanneke, S. Fogwell, and G. Gabrielse, “New Measurement of the Electron Magnetic
307 Moment and the Fine Structure Constant”, *Phys. Rev. Lett.* **100** (2008) 120801,
308 doi:10.1103/PhysRevLett.100.120801, arXiv:0801.1134.
- 309 [31] L. Forthomme (Wikimedia Commons), “File:Cern-accelerator-complex.svg — Wikimedia
310 Commons, the free media repository”,
311 <https://commons.wikimedia.org/wiki/File:Cern-accelerator-complex.svg>, 2016.
312 (Retrieved Jul 24, 2017).
- 313 [32] S. Holmes, R. S. Moore, and V. Shiltsev, “Overview of the Tevatron Collider Complex:
314 Goals, Operations and Performance”, *JINST* **6** (2011) T08001,
315 doi:10.1088/1748-0221/6/08/T08001, arXiv:1106.0909.
- 316 [33] L. Evans and P. Bryant, “LHC Machine”, *JINST* **3** (2008), no. 08, S08001,
317 doi:10.1088/1748-0221/3/08/S08001.
- 318 [34] CMS Collaboration, “Public CMS Luminosity Information”.
319 <https://twiki.cern.ch/twiki/bin/view/CMSPublic/LumiPublicResults>. (Retrieved
320 Dec 6, 2022).
- 321 [35] I. Efthymiopoulos et al., “Bunch Luminosity Variations in LHC Run 2. BUNCH
322 LUMINOSITY VARIATIONS IN LHC RUN 2”, *JACoW IPAC* **2021** (2021) 4094,
323 doi:10.18429/JACoW-IPAC2021-THPAB172.
- 324 [36] CMS Collaboration, “The CMS experiment at the CERN LHC”, *JINST* **3** (2008)
325 S08004, doi:10.1088/1748-0221/3/08/S08004.
- 326 [37] Neutelings, Izaak, “CMS coordinate system – TikZ.net”,
327 https://tikz.net/axis3d_cms/, 2022. (Retrieved Dec 2, 2022).
- 328 [38] Neutelings, Izaak, “Pseudorapidity – TikZ.net”,
329 https://tikz.net/axis2d_pseudorapidity/, 2022. (Retrieved Dec 2, 2022).
- 330 [39] CMS Collaboration, “Performance of the CMS Drift Tube Chambers with Cosmic Rays”,
331 *JINST* **5** (2010) T03015, doi:10.1088/1748-0221/5/03/T03015, arXiv:0911.4855.
- 332 [40] CMS Collaboration, “CMS Tracker Detector Performance Results”,
333 <https://twiki.cern.ch/twiki/bin/view/CMSPublic/DPGResultsTRK>, 2022.
334 (Retrieved Dec 2, 2022).
- 335 [41] CMS Tracker Group, “The CMS Phase-1 Pixel Detector Upgrade”, *JINST* **16** (2021),
336 no. 02, P02027, doi:10.1088/1748-0221/16/02/P02027, arXiv:2012.14304.
- 337 [42] CMS Collaboration, “Precise Mapping of the Magnetic Field in the CMS Barrel Yoke
338 using Cosmic Rays”, *JINST* **5** (2015) T03021, doi:10.1088/1748-0221/5/03/T03021,
339 arXiv:0910.5530.
- 340 [43] CMS Collaboration, “Description and performance of track and primary-vertex
341 reconstruction with the CMS tracker”, *JINST* **9** (2014) P10009,
342 doi:10.1088/1748-0221/9/10/P10009, arXiv:1405.6569.

- 343 [44] **CMS** Collaboration, “The Phase-1 upgrade of the CMS pixel detector”, *JINST* **12**
 344 (2017), no. 07, C07009, doi:10.1088/1748-0221/12/07/C07009.
- 345 [45] **CMS** Collaboration, “CMS Tracking POG Performance Plots For 2017 with PhaseI
 346 pixel detector”, [https://twiki.cern.ch/twiki/bin/view/CMSPublic/
 347 TrackingPOGPerformance2017MC#Vertex_Resolutions](https://twiki.cern.ch/twiki/bin/view/CMSPublic/TrackingPOGPerformance2017MC#Vertex_Resolutions), 2022. (Retrieved Dec 8, 2022).
- 348 [46] **CMS** Collaboration, “The CMS electromagnetic calorimeter project: Technical Design
 349 Report”, Technical Design Report CMS. CERN, Geneva, 1997.
- 350 [47] **CMS** Collaboration, “Jet energy scale and resolution in the CMS experiment in pp
 351 collisions at 8 TeV”, *JINST* **12** (2017), no. 02, P02014,
 352 doi:10.1088/1748-0221/12/02/P02014, arXiv:1607.03663.
- 353 [48] E. Manca, “Validation of the muon momentum resolution in view of the W mass
 354 measurement with the CMS experiment”. PhD thesis, INFN, Pisa, 2016.
 355 CMS-TS-2016-024, CERN-THESIS-2016-173.
- 356 [49] **CMS** Collaboration, “The CMS muon project : Technical Design Report”, Technical
 357 Design Report CMS. CERN, Geneva, 1997.
- 358 [50] **CMS** Collaboration, “The CMS trigger system”, *JINST* **12** (2017) P01020,
 359 doi:10.1088/1748-0221/12/01/P01020, arXiv:1609.02366.
- 360 [51] L. Lee, C. Ohm, A. Soffer, and T.-T. Yu, “Collider Searches for Long-Lived Particles
 361 Beyond the Standard Model”, *Prog. Part. Nucl. Phys.* **106** (2019) 210,
 362 doi:10.1016/j.ppnp.2019.02.006, arXiv:1810.12602. [Erratum:
 363 *Prog.Part.Nucl.Phys.* 122, 103912 (2022)].
- 364 [52] D. Barney, “CMS Slice”, <https://cds.cern.ch/record/2628641/>, 2015. (Retrieved
 365 Dec 8, 2022).
- 366 [53] **CMS** Collaboration, “Commissioning of the Particle-flow Event Reconstruction with the
 367 first LHC collisions recorded in the CMS detector”, CMS Physics Analysis Summary
 368 CMS-PAS-PFT-10-001, CERN, 2010.
- 369 [54] **CMS** Collaboration, “Particle-flow reconstruction and global event description with the
 370 CMS detector”, *JINST* **12** (2017) P10003, doi:10.1088/1748-0221/12/10/P10003,
 371 arXiv:1706.04965.
- 372 [55] W. Adam, B. Mangano, T. Speer, and T. Todorov, “Track Reconstruction in the CMS
 373 tracker”, technical report, CERN, Geneva, 2006.
- 374 [56] R. Frühwirth, “Application of Kalman filtering to track and vertex fitting”, *Nucl.
 375 Instrum. Meth. A* **262** (1987) 444, doi:10.1016/0168-9002(87)90887-4.
- 376 [57] K. Rose, “Deterministic annealing for clustering, compression, classification, regression,
 377 and related optimization problems”, *IEEE Proc.* **86** (1998), no. 11, 2210,
 378 doi:10.1109/5.726788.
- 379 [58] R. Frühwirth, W. Waltenberger, and P. Vanlaer, “Adaptive Vertex Fitting”, technical
 380 report, CERN, Geneva, 2007.
- 381 [59] **CMS** Collaboration, “Technical proposal for the Phase-II upgrade of the Compact Muon
 382 Solenoid”, CMS Technical Proposal CERN-LHCC-2015-010, CMS-TDR-15-02, CERN,

- 383 2015.
- 384 [60] W. Adam, R. Fröhwirth, A. Strandlie, and T. Todorov, “Reconstruction of electrons with
 385 the Gaussian-sum filter in the CMS tracker at the LHC”, *Journal of Physics G: Nuclear
 386 and Particle Physics* **31** (2005), no. 9, N9, doi:10.1088/0954-3899/31/9/n01.
- 387 [61] **CMS** Collaboration, “Electron and photon reconstruction and identification with the
 388 CMS experiment at the CERN LHC”, *JINST* **16** (2021) P05014,
 389 doi:10.1088/1748-0221/16/05/P05014, arXiv:2012.06888.
- 390 [62] **CMS** Collaboration, “ECAL 2016 refined calibration and Run2 summary plots”, CMS
 391 Detector Performance Summary CMS-DP-2020-021, CERN, 2020.
- 392 [63] **CMS** Collaboration, “Performance of electron reconstruction and selection with the
 393 CMS detector in proton-proton collisions at $\sqrt{s} = 8$ TeV”, *JINST* **10** (2015) P06005,
 394 doi:10.1088/1748-0221/10/06/P06005, arXiv:1502.02701.
- 395 [64] M. Cacciari and G. P. Salam, “Pileup subtraction using jet areas”, *Phys. Lett. B* **659**
 396 (2008) 119, doi:10.1016/j.physletb.2007.09.077, arXiv:0707.1378.
- 397 [65] **CMS** Collaboration, “Performance of the CMS muon detector and muon reconstruction
 398 with proton-proton collisions at $\sqrt{s} = 13$ TeV”, *JINST* **13** (2018) P06015,
 399 doi:10.1088/1748-0221/13/06/P06015, arXiv:1804.04528.
- 400 [66] **CMS** Collaboration, “Performance of τ -lepton reconstruction and identification in
 401 CMS”, *JINST* **7** (2012), no. 01, P01001, doi:10.1088/1748-0221/7/01/P01001,
 402 arXiv:1109.6034.
- 403 [67] **CMS** Collaboration, “Performance of reconstruction and identification of τ leptons
 404 decaying to hadrons and ν_τ in pp collisions at $\sqrt{s} = 13$ TeV”, *JINST* **13** (2018) P10005,
 405 doi:10.1088/1748-0221/13/10/P10005, arXiv:1809.02816.
- 406 [68] **CMS** Collaboration, “Performance of reconstruction and identification of tau leptons in
 407 their decays to hadrons and tau neutrino in LHC Run-2”, CMS Physics Analysis
 408 Summary CMS-PAS-TAU-16-002, CERN, 2016.
- 409 [69] **CMS** Collaboration, “Identification of hadronic tau lepton decays using a deep neural
 410 network”, *JINST* **17** (2022), no. 07, P07023, doi:10.1088/1748-0221/17/07/p07023,
 411 arXiv:2201.08458.
- 412 [70] Y. Takahashi and M. Tomoto, “Measurement of the top-quark pair production
 413 cross-section in pp collisions at $\sqrt{s} = 7$ TeV using final states with an electron or a muon
 414 and a hadronically decaying τ -lepton”. PhD thesis, Nagoya University, 2012.
 415 CERN-THESIS-2012-252.
- 416 [71] M. Cacciari, G. P. Salam, and G. Soyez, “The anti- k_T jet clustering algorithm”, *JHEP*
 417 **04** (2008) 063, doi:10.1088/1126-6708/2008/04/063, arXiv:0802.1189.
- 418 [72] M. Cacciari and G. P. Salam, “Dispelling the N^3 myth for the k_T jet-finder”, *Phys. Lett.*
 419 *B* **641** (2006) 57, doi:10.1016/j.physletb.2006.08.037, arXiv:hep-ph/0512210.
- 420 [73] M. Cacciari, G. P. Salam, and G. Soyez, “FastJet user manual”, *Eur. Phys. J. C* **72**
 421 (2012) 1896, doi:10.1140/epjc/s10052-012-1896-2, arXiv:1111.6097.
- 422 [74] **CMS** Collaboration, “Determination of jet energy calibration and transverse momentum

- resolution in CMS”, *JINST* **6** (2011) P11002, doi:10.1088/1748-0221/6/11/P11002, arXiv:1107.4277.
- [75] CMS Collaboration, “Pileup Jet Identification”, CMS Physics Analysis Summary CMS-PAS-JME-13-005, CERN, 2013.
- [76] CMS Collaboration, “Jet algorithms performance in 13 TeV data”, CMS Physics Analysis Summary CMS-PAS-JME-16-003, CERN, 2017.
- [77] D. Guest et al., “Jet Flavor Classification in High-Energy Physics with Deep Neural Networks”, *Phys. Rev. D* **94** (2016), no. 11, 112002, doi:10.1103/PhysRevD.94.112002, arXiv:1607.08633.
- [78] CMS Collaboration, “Identification of heavy-flavour jets with the CMS detector in pp collisions at 13 TeV”, *JINST* **13** (2018), no. 05, P05011, doi:10.1088/1748-0221/13/05/P05011, arXiv:1712.07158.
- [79] CMS Collaboration, “Performance of missing energy reconstruction in 13 TeV pp collision data using the CMS detector”, CMS Physics Analysis Summary CMS-PAS-JME-16-004, CERN, 2016.
- [80] CMS Collaboration, “Performance of missing transverse momentum in pp collisions at $\sqrt{s} = 13$ TeV using the CMS detector”, CMS Physics Analysis Summary CMS-PAS-JME-17-001, CERN, 2018.
- [81] SLAC Collaboration, “Simulations”.
<https://theory.slac.stanford.edu/our-research/simulations>. (Retrieved Jul 25, 2017).
- [82] CMS Collaboration, “Event generator tunes obtained from underlying event and multiparton scattering measurements”, *Eur. Phys. J. C* **76** (2016) 155, doi:10.1140/epjc/s10052-016-3988-x, arXiv:1512.00815.
- [83] CMS Collaboration, “Extraction and validation of a new set of CMS PYTHIA8 tunes from underlying-event measurements”, *Eur. Phys. J. C* **80** (2020) 4, doi:10.1140/epjc/s10052-019-7499-4, arXiv:1903.12179.
- [84] CMS Collaboration, “Investigations of the impact of the parton shower tuning in Pythia 8 in the modelling of $t\bar{t}$ at $\sqrt{s} = 8$ and 13 TeV”, CMS Physics Analysis Summary CMS-PAS-TOP-16-021, CERN, 2016.
- [85] GEANT4 Collaboration, “GEANT4 — a simulation toolkit”, *Nucl. Instrum. Meth. A* **506** (2003) 250, doi:10.1016/S0168-9002(03)01368-8.
- [86] M. H. Seymour and M. Marx, “Monte Carlo Event Generators”, in *Proceedings, 69th Scottish Universities Summer School in Physics: LHC Phenomenology (SUSSP69) 2012*, p. 287. St.Andrews, Scotland, U.K., 2013. arXiv:1304.6677. doi:10.1007/978-3-319-05362-2_8.
- [87] T. Sjöstrand, S. Mrenna, and P. Z. Skands, “PYTHIA 6.4 Physics and Manual”, *JHEP* **05** (2006) 026, doi:10.1088/1126-6708/2006/05/026, arXiv:hep-ph/0603175.
- [88] F. Maltoni and T. Stelzer, “MadEvent: Automatic event generation with MadGraph”, *JHEP* **02** (2003) 027, doi:10.1088/1126-6708/2003/02/027, arXiv:hep-ph/0208156.

- 463 [89] J. Alwall et al., “Comparative study of various algorithms for the merging of parton
 464 showers and matrix elements in hadronic collisions”, *Eur. Phys. J. C* **53** (2008) 473,
 465 doi:10.1140/epjc/s10052-007-0490-5, arXiv:0706.2569.
- 466 [90] J. Alwall et al., “The automated computation of tree-level and next-to-leading order
 467 differential cross sections, and their matching to parton shower simulations”, *JHEP* **07**
 468 (2014) 079, doi:10.1007/JHEP07(2014)079, arXiv:1405.0301.
- 469 [91] P. Nason, “A new method for combining NLO QCD with shower Monte Carlo
 470 algorithms”, *JHEP* **11** (2004) 040, doi:10.1088/1126-6708/2004/11/040,
 471 arXiv:hep-ph/0409146.
- 472 [92] S. Frixione, P. Nason, and C. Oleari, “Matching NLO QCD computations with parton
 473 shower simulations: the POWHEG method”, *JHEP* **11** (2007) 070,
 474 doi:10.1088/1126-6708/2007/11/070, arXiv:0709.2092.
- 475 [93] S. Alioli, P. Nason, C. Oleari, and E. Re, “A general framework for implementing NLO
 476 calculations in shower Monte Carlo programs: the POWHEG BOX”, *JHEP* **06** (2010)
 477 043, doi:10.1007/JHEP06(2010)043, arXiv:1002.2581.
- 478 [94] S. Frixione, P. Nason, and G. Ridolfi, “A positive-weight next-to-leading-order Monte
 479 Carlo for heavy flavour hadroproduction”, *JHEP* **09** (2007) 126,
 480 doi:10.1088/1126-6708/2007/09/126, arXiv:0707.3088.
- 481 [95] J. M. Campbell, R. K. Ellis, P. Nason, and E. Re, “Top-Pair Production and Decay at
 482 NLO Matched with Parton Showers”, *JHEP* **04** (2015) 114,
 483 doi:10.1007/JHEP04(2015)114, arXiv:1412.1828.
- 484 [96] S. Alioli, P. Nason, C. Oleari, and E. Re, “NLO single-top production matched with
 485 shower in POWHEG: s - and t -channel contributions”, *JHEP* **09** (2009) 111,
 486 doi:10.1088/1126-6708/2009/09/111, arXiv:0907.4076. [Erratum:
 487 doi:10.1007/JHEP02(2010)011].
- 488 [97] E. Re, “Single-top Wt-channel production matched with parton showers using the
 489 POWHEG method”, *Eur. Phys. J. C* **71** (2011) 1547,
 490 doi:10.1140/epjc/s10052-011-1547-z, arXiv:1009.2450.
- 491 [98] T. Sjöstrand, S. Mrenna, and Z. S., Peter, “A Brief Introduction to PYTHIA 8.1”,
 492 *Comput. Phys. Commun.* **178** (2008) 852, doi:10.1016/j.cpc.2008.01.036,
 493 arXiv:0710.3820.
- 494 [99] T. Sjöstrand et al., “An introduction to PYTHIA 8.2”, *Comput. Phys. Commun.* **191**
 495 (2015) 159, doi:10.1016/j.cpc.2015.01.024, arXiv:1410.3012.
- 496 [100] R. D. Ball et al., “Parton distributions for the LHC Run II”, *JHEP* **15** (2015) 40,
 497 doi:10.1007/JHEP04(2015)040, arXiv:1410.8849.
- 498 [101] K. Melnikov and F. Petriello, “Electroweak gauge boson production at hadron colliders
 499 through $O(\alpha(s)^{**2})$ ”, *Phys.Rev. D* **74** (2006) 114017,
 500 doi:10.1103/PhysRevD.74.114017, arXiv:hep-ph/0609070.
- 501 [102] M. Czakon and A. Mitov, “Top++: A Program for the Calculation of the Top-Pair
 502 Cross-Section at Hadron Colliders”, *Comput. Phys. Commun.* **185** (2014) 2930,
 503 doi:10.1016/j.cpc.2014.06.021, arXiv:1112.5675.

504 [103] “NNLO+NNLL top-quark-pair cross sections – ATLAS-CMS recommended predictions
505 for top-quark-pair cross sections using the Top++v2.0 program (M. Czakon, A. Mitov,
506 2013)”, <https://twiki.cern.ch/twiki/bin/view/LHCPhysics/TtbarNNLO>, 2022.
507 (Retrieved Dec 21, 2020).